Thermal energy harvesting circuit with maximum power point tracking control for self-powered sensor node applications[*]

Eun-Jung YOON, Jong-Tae PARK, Chong-Gun YU[‡]

Department of Electronics Engineering, Incheon National University, Incheon 406-772, Korea

E-mail: ngkorea@nate.com; jtpark@inu.ac.kr; chong@inu.ac.kr

Abstract: We present a simple implementation of a thermal energy harvesting circuit with the maximum power point tracking (MPPT) control for self-powered miniature-sized sensor nodes. Complex start-up circuitry and direct current to direct current (DC-DC) boost converters are not required, because the output voltage of targeted thermoelectric generator (TEG) devices is high enough to drive the load applications directly. The circuit operates in the active/asleep mode to overcome the power mismatch between TEG devices and load applications. The proposed circuit was implemented using a 0.35-μm complementary metal-oxide semiconductor (CMOS) process. Experimental results confirmed correct circuit operation and demonstrated the performance of the MPPT scheme. The circuit achieved a peak power efficiency of 95.5% and an MPPT accuracy of higher than 99%.

Key words: Thermoelectric energy; Energy harvesting; Maximum power point tracking (MPPT) control; Self-powered system; Sensor node

1 Introduction

Wireless sensor applications, such as the Internet of Things, ambient intelligence, and wireless sensor networks, have become popular subjects of active research and development, within the scope of the ever-present attempt to increase the amount of information transfer among humans, objects, and environments (Belleville et al., 2010; Kausar et al., 2014; Morimura et al., 2014). These applications require high integration levels, compact volumes, low costs, and near-perpetual operations. The key challenge for these systems is to provide completely independent, lightweight, and miniature-sized power sources, with long lifetimes, to drive the sensor nodes. In the conventional electrochemical battery approach,

battery capacity is limited by the extreme constraints on system size. More importantly, battery recharge or replacement in applications such as implantable bio-devices or wireless sensor networks is not practical or may even be cost-prohibitive. To solve this problem, energy harvesting technologies (Colomer-Farrarons et al., 2008; Lhermet et al., 2008; Doms et al., 2009; Carlson et al., 2010; Chen et al., 2011a, 2011b; Lu et al., 2011; Ramadass and Chandrakasan, 2011; Im et al., 2012; Kim and Kim, 2013; Weng et al., 2013; Yoon and Yu, 2016) have gained much attention as a mean to avoid using batteries.

Recently, miniature-sized sensor nodes have been developed for various applications, such as condition monitoring, medical diagnosis, and environmental monitoring (Table 1). Advances in device manufacturing, packaging technologies, low-voltage low-power circuit design techniques, and wireless transmission methods are creating opportunities to reduce size, power, and cost of wireless sensor nodes dramatically without affecting the device lifetime. These millimeter-scale sensor nodes use energy

---

Table 1 Summary of state-of-the-art miniature-sized sensor nodes

Research	Technology (nm)	Power source	Supply voltage (V)	Sensor		MCU
				Type	Interface	
Jang et al. (2013)	130	Vibration	0.93–1	Capacitive resistive	Semi-digital (PWM)	–
Zhang et al. (2013)	130	Thermal, RF	0.5, 1.0, 1.2	ECG, EMG, EEG	8-bit ADC	8-bit RISC ISA
Arsalan et al. (2013)	180	RF	>1.0	Temperature pressure	7-bit ADC	–
Lee et al. (2013)	65/130/180	TFB, solar	0.6, 1.2	Temperature image	8-bit ADC	ARM Cortex-M0
Kim et al. (2015)	130/180	TFB, solar	0.6, 1.2	Temperature	13-bit CDC	ARM Cortex-M0
Mansano et al. (2016)	180	RF	1.25	ECG	8-bit ADC	–

Research	Radio		Active time (ms)	Size	Power		Application
	Rx	Tx			Active	Standby (nW)	
Jang et al. (2013)	2.6 GHz OOK	3.2 GHz BPSK	20	2.4 mm^2	85.5 μW	–	Condition monitoring
Zhang et al. (2013)	–	402/433 MHz BFSK	21	8.25 mm^2	19 μW	–	BSN
Arsalan et al. (2013)	5.2 GHz OOK	2.4 GHz OOK		1.4 mm^3	513 μW (peak)	–	IOPM
Lee et al. (2013)	GOC	GOC	100	1.0 mm^3	<5 μA >10 μA (Tx: on)	11	General
Kim et al. (2015)	–	8 GHz UWB	700	10.6 mm^3	36 μW	8	General
Mansano et al. (2016)	–	402 MHz OOK		3.8 mm^2	9.7 μW	–	ECG monitoring

TFB: thin film battery; GOC: global optical communication; IOPM: intraocular pressure monitoring; CDC: capacitance-to-digital converter; ECG: electrocardiogram; EMG: electromyogram; EEG: electroencephalogram; BSN: body sensor node

harvested from available ambient sources, such as light, vibrations, thermal imbalances, and radio frequency waves, to reduce maintenance costs for battery replacement or recharging. Thermal energy often appears as losses during other energy conversion processes and is amenable to energy harvesting in our daily life, in the form of temperature gradients or heat flows. Miniaturized thermoelectric generator (TEG) devices for micro-scale energy harvesting (Strasser et al., 2003; Leonov et al., 2005; Tellurex (http://www.tellurex.com); Micropelt, 2018; Thermo Life (http://www.poweredbythermolife.com/corp.htm)) have been successfully fabricated using recent advances in semiconductor process technology.

The energy transducers in miniature sensor nodes are limited in size; therefore, the resulting energy harvesting produces a relatively small amount of power. Moreover, the energy sources can be very unsteady; they are often irregular or intermittent. The power required to operate the sensor nodes is usually greater than the power harvested by miniature energy transducers. An efficient power management system is therefore needed to solve the resulting power mismatch. Recently, the active/asleep technique has been used in energy harvesting systems to overcome this problem (Colomer-Farrarons et al., 2008; Lu et al., 2011; Yoon and Yu, 2016). With this technique, the system is active when there is sufficient energy and asleep when there is not. The operation duty cycle depends on how much energy the system can harvest. Implementing this technique is simple; therefore, it is fit for self-powered sensor nodes with low duty-cycle sensing or monitoring applications.

The commonly used TEG devices can generate low output voltages 10–50 mV/K (Ramadass and Chandrakasan, 2011; Im et al., 2012; Kim and Kim, 2013; Weng et al., 2013). Therefore, a boost converter is needed to provide the output voltage required for

powering electronic devices. Most research focused on thermal energy harvesting used the low-output-voltage TEG devices. Therefore, the focus has been on start-up and direct current to direct current (DC-DC) boosting issues. Several start-up techniques have been reported using pre-charged batteries (Doms et al., 2009; Carlson et al., 2010), mechanical switches (Ramadass and Chandrakasan, 2011), off-chip transformers (Im et al., 2012), LC oscillators (Weng et al., 2013), or post-fabrication processes (Chen et al., 2011a). The techniques proposed by Doms et al. (2009) and Carlson et al. (2010) are not applicable to battery-free self-powered sensor nodes. The techniques proposed by Ramadass and Chandrakasan (2011), Im et al. (2012), and Weng et al. (2013) are not suitable for system integration or miniaturization. The technique proposed by Chen et al. (2011a) requires threshold voltage tuning after fabrication; hence, it is not applicable to standard, foundry provided, complementary metal-oxide semiconductor (CMOS) technologies. These techniques are therefore not suitable for self-powered miniature-sized sensor node applications. For DC-DC boosting, a charge pump using a switched-capacitor technique has been used by Doms et al. (2009). DC-DC boost converters using switched-inductor techniques (Lhermet et al., 2008; Carlson et al., 2010; Chen et al., 2011a, 2011b; Ramadass and Chandrakasan, 2011; Im et al., 2012; Kim and Kim, 2013; Weng et al., 2013) have been popular because of their better conversion efficiency characteristics. However, these techniques require to use an external inductor (Lhermet et al., 2008; Carlson et al., 2010; Chen et al., 2011a; Im et al., 2012; Kim and Kim, 2013) or even three inductors (Ramadass and Chandrakasan, 2011; Weng et al., 2013), which places additional burden on system miniaturization.

TEG devices with high output voltages have also been developed. Micro-machined TEG devices (Leonov et al., 2005) can generate output voltages 1–8 V at an ambient room temperature. Commercial TEG devices (Thermo Life, http://www.poweredbythermolife.com/corp.htm) can generate nearly 6 V of open voltage with temperature difference (ΔT) less than 5 °C. With the high-voltage TEG devices, start-up and DC-DC boosting issues can be solved, and the implementation of thermal energy harvesting systems can hence be greatly simplified, which makes these systems suitable to be used in self-powered miniature-sized sensor nodes.

Using these devices, the main remaining design issue is the maximum power point tracking (MPPT) capability. MPPT techniques using digital signal processing usually require considerable power consumption (Kim and Lai, 2008), which makes them impractical in micro-energy harvesting systems. An impedance matching technique was used by Ramadass and Chandrakasan (2011) and Weng et al. (2013) as a very simple and low-power MPPT method. In this method, the switching frequency of a boost converter is determined by the internal resistance (R_T) of the TEG device and the inductor value (L) of the boost converter. However, R_T of a TEG device depends on ΔT and can deviate by 12% from the nominal value (Kim and Kim, 2013), and the inductance of a general inductor has a tolerance of at least ±20%. Moreover, the frequency generated from on-chip clock oscillators varies over a wide range depending on the process, voltage, and temperature. Therefore, this technique cannot effectively track the maximum power point (MPP). Another simple low-power MPPT method is fractional open-circuit voltage (FOC) (Im et al., 2012; Kim and Kim, 2013). The open-circuit voltage (V_{OC}) is sampled periodically to determine V_{MPP}, which is half of V_{OC}, by electrically disconnecting the TEG device by a switch or shutting off the power converter.

In this study we propose a simple implementation technique for a thermal energy harvesting circuit designed for TEG devices with high output voltage, with application in self-powered miniature-sized sensor nodes. The output voltage of targeted TEG devices is high enough to drive load applications directly; therefore, no complex start-up circuitry is required. Moreover, the need for a DC-DC boost converter can be removed using the active/asleep technique in system operation. A simple MPPT controller using the FOC technique is proposed to extract as much power as possible from the TEG device while minimizing the power overhead introduced by the controller.

2 Thermoelectric generators

A TEG converts thermal energy in the form of ΔT into electrical energy, based on the Seebeck effect. The basic unit of a TEG is a thermocouple, which is

composed of n- and p-doped semiconductor pellets connected electrically in series and thermally in parallel. When a temperature gradient is established across this material, heat begins to flow from the hot side to the cold side. Both electrons and holes are moving from the hot side to the cold side by the flow of heat, creating an electric potential and therefore causing a current to flow if a load is connected to the TEG's terminals.

A TEG can effectively be modeled by a voltage source V_T in series with an R_T (Fig. 1). The magnitude of V_{OC} depends on the material and varies with temperature. It can be expressed as

$$V_{oc} = V_T = \alpha N_{couple} \Delta T, \qquad (1)$$

where α is the Seebeck coefficient, N_{couple} the number of thermocouples, and ΔT the temperature difference applied across the harvester. R_T is the sum of resistance along the pellet bodies and their interconnections, and varies slightly with the average temperature of the TEG. Because of the linear I-V

characteristics of the TEG, the MPP voltage (V_{MPP}) and maximum available power (P_{max}) of the TEG can be easily derived as

$$V_{MPP} = \frac{1}{2} V_{OC}, \quad P_{max} = \frac{V_{OC}^2}{4R_T}. \qquad (2)$$

Characteristics of several TEG devices (including commercial TEGs) are compared in Table 2. Currently, most commercial TEGs use bismuth telluride as the thermoelectric material, because of its superior thermoelectric properties. Micro-machined TEG devices (Leonov et al., 2005) can generate output voltages 1–8 V at an ambient room temperature. R_T ranges from 20 kΩ to 3 MΩ. The available power varies in 5–30 µW/cm^2 for a TEG worn on a body at the room temperature. Commercial TEG devices such as Thermo Life can generate nearly 6 V of open voltage at ΔT<5 °C, with an available power of 30 µW and a volume of 0.2 cm^3.

In this study, we used a TEG model with V_T=3 V and R_T=15 kΩ for the experiment. This is equivalent
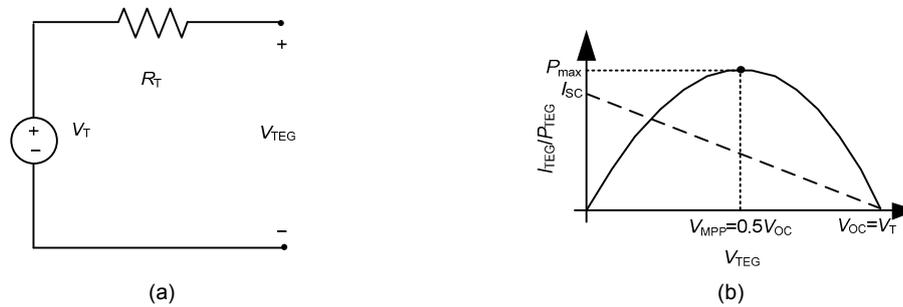

Fig. 1 A targeted thermoelectric generator modeled by voltage source (V_T) and internal resistance (R_T): (a) an equivalent circuit of a TEG; (b) I-V and P-V characteristics of a TEG

Table 2 Characteristics of TEG devices

Research	Material	TEG characteristics	Size	Operating temperature range (optimal temperature)	Model
Strasser et al. (2003)	poly-Si	V_{oc}=10 V/cm^2, P_{max}=1 µW/cm^2 @ ΔT=5 K	–	–	–
Leonov et al. (2005)	Bi-Te	V_{oc}=1–8 V/cm^2, P_{max}=30 µW/cm^2 @ ΔT=2–3 K, R_T=20 kΩ–3 MΩ	–	–	–
Tellurex	Bi-Te	V_{oc}=10.8 V, P_{max}=5.4 W @ ΔT=300 K, R_T=5.4 Ω	30 mm×30 mm× 4.3 mm	≤400 °C (200–250 °C)	G2-30-0313
Micropelt (2018)	Bi-Te	V_{oc}=0.4 V, P_{max}=150 µW @ ΔT=5 K, R_T=210 Ω	2.4 mm×3.3 mm× 1.1 mm	0–70 °C (27 °C)	MPG-D655
Thermo Life	Bi-Te	V_{oc}=6 V, P_{max}=30 µW @ ΔT=5 K, R_T=300 kΩ	Diameter: 9.3 mm; height: 1.4 mm	0–100 °C (20–25 °C)	Thermo Life

to 17 commercial Thermo Life TEGs wired in parallel. We also tested our circuit with TEG models with increased R_T. The maximum value of R_T when the designed circuit works properly is 100 kΩ, equivalent to three Thermo Life TEGs wired in parallel.

3 The proposed thermal energy harvesting circuit

3.1 Overall circuit description

The proposed thermal energy harvesting circuit consists of a TEG device, an MPPT control block, two p-type metal-oxide-semiconductor (PMOS) switches (SW1, SW2), and a storage capacitor (C_{STO}) (Fig. 2). The circuit operates in active/asleep mode. The application load switches between active and asleep modes depending on the harvested energy. The operation duty cycle depends on how much energy the circuit can harvest. To track the MPP, load matching is achieved by adaptively connecting the C_{STO} to the load, turning SW2 on or off. When the energy stored in C_{STO} is transferred to the load, the application load is triggered and woken up to start an atomic operation.
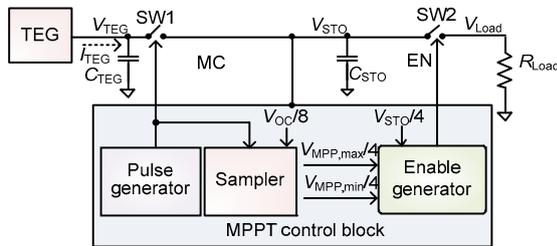
Fig. 2 Block diagram of the proposed thermal energy harvesting circuit

Thermoelectric energy is transduced into electrical energy by TEG devices. MPPT controls MPP of TEG and transfers the harvested energy to the load. The block consists of a pulse generator, a sampler, and an enable generator circuit. The pulse generator shown in Fig. 3 is used to generate an MPPT pulse (MC) for MPPT control. MC pulse is one cycle long for every 128 cycles of the clock signal (CLK) and is generated using a ring-type oscillator (Fig. 4). The frequency of CLK is 250 Hz. During this cycle (MC=1), SW1 is open and the sampler evaluates TEG

V_{OC}. The enable generator circuit compares sampled data with supply voltage (V_{STO}) to produce the control signal (EN), determining the on/off state of SW2. A band-band control scheme is employed to maintain V_{STO} at approximately V_{MPP} for load matching.
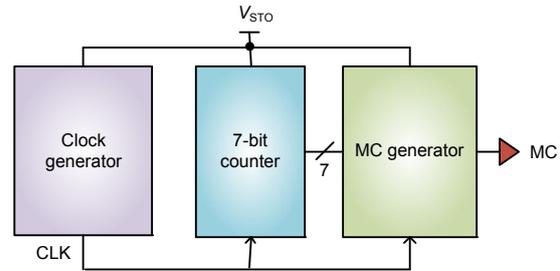

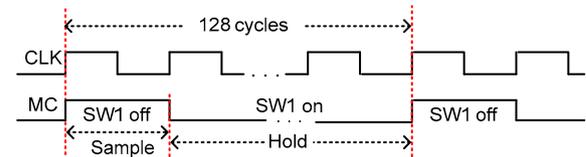**Fig. 3 Block diagram of the pulse generator**

Fig. 4 Timing diagram of the CLK and MPPT pulse (MC)

3.2 Sampler

The architecture of the designed sampler is shown in Fig. 5. When MC is high, PMOS SW1 is open, and n-type metal-oxide-semiconductor (NMOS) switches SW3 and SW4 are closed. Therefore, the TEG is disconnected from C_{STO}, and the sampler evaluates TEG V_{OC}. In practice, $V_{OC}/8$ is sampled instead of $V_{OC}/2$, which equals V_{MPP}, using a resistor string for proper operation of internal circuits. The total resistance of the resistor string is high enough to justify, ignoring the current in the resistor string.

A two-stage sample and hold (S/H) architecture (Seeman et al., 2008) is employed to reduce leakage and to maintain the sampled voltage during the long hold times. The first sampling capacitor discharges linearly to the input, but the second capacitor discharges depending on the difference between the two capacitor voltages, forming a quadratic voltage profile. Therefore, for a given sample rate, the S/H topology is more space-efficient than a single-stage circuit using a larger capacitor.

Simulation results using 0.35-μm CMOS process parameters have demonstrated that the discharge voltage during the hold time of the designed sampler

with two sampling capacitors ($C_{SH1}=C_{SH2}=20$ pF) is 187 μV, whereas that of the single-stage sampler with a sampling capacitance of 40 pF is 5 mV. This means that with a two-stage topology, the capacitance required for the same discharge voltage is reduced by about 96.3%.
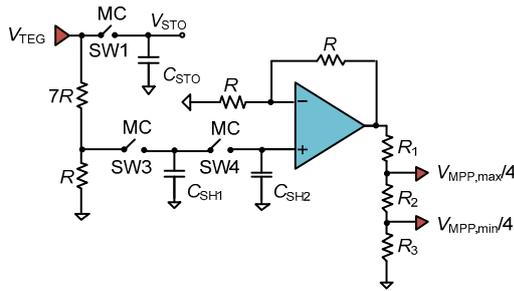

Fig. 5 Sampler architecture

Two reference MPP voltages, $V_{MPP,max}/4$ and $V_{MPP,min}/4$, are generated using a noninverting amplifier and another resistor string (R_1, R_2, and R_3). $V_{MPP,max}$ and $V_{MPP,min}$ are designed to have values of $V_{MPP}+\alpha$ and $V_{MPP}-\alpha$, respectively. The value of α is small and its specific value is not critical for band-band control. In this design, the value of α is about 5.3% of V_{MPP}.

A conventional two-stage topology with pole-zero cancellation was chosen for the amplifier (Fig. 6). To supply the amplifier with a constant bias current even in the presence of a changing V_{STO}, a reference circuit based on a full MOSFET bandgap architecture (Cheng and Wu, 2005) was designed. The reference circuit (Fig. 7) includes a start-up circuit (Li et al., 2009) which consumes no power after start-up.
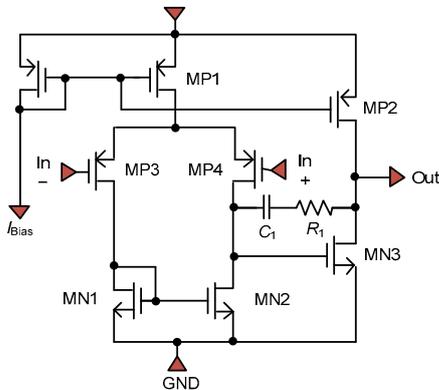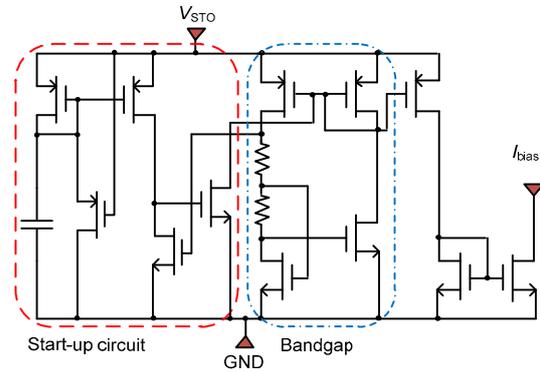

Fig. 6 Schematic of the two-stage amplifier

Fig. 7 Schematic of the reference circuit

3.3 Enable generator circuit

The enable generator circuit consists of two comparators and a latch (Fig. 8). The upper comparator detects whether the voltage on the C_{STO} ($V_{STO}/4$, in practice) reaches the predetermined maximum MPP level, $V_{MPP,max}/4$, while the lower one detects whether it reaches the predetermined minimum MPP level, $V_{MPP,min}/4$. The signals generated by the comparators are used by the latch to generate EN that determines the on/off state of PMOS SW2, thus defining the charge and discharge phases.
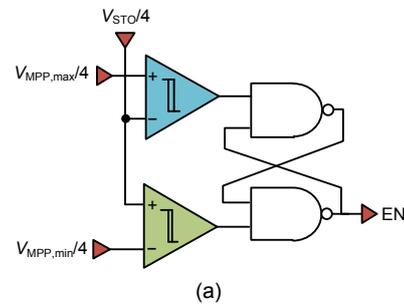

Fig. 8 Enable generator circuit (a) and timing diagram of band-band control (b)

When C_{STO} is charged to $V_{MPP,max}$, EN becomes low and turns on SW2, waking up the load application from asleep mode. Power stored on C_{STO} is delivered to the load during the discharge phase. When C_{STO} is discharged down to $V_{MPP,min}$, EN becomes high and turns off SW2. Power transfer to the load stops and one operation cycle is finished. Later on, when the harvested power charges C_{STO}, the operation cycle repeats. Therefore, C_{STO} is repeatedly charged and discharged around V_{MPP}, and TEG always operates near its MPP.

To define the voltage detection levels better, the comparators have been designed with a hysteresis of 20 mV. A schematic of the designed comparators is shown in Fig. 9. These two comparators share the same reference circuit of Fig. 7 used in the sampler amplifier.
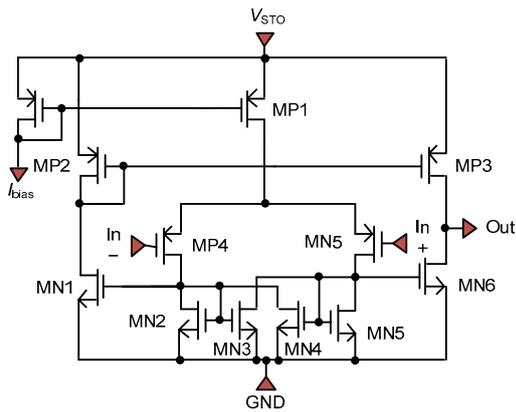

Fig. 9 Schematic of the comparator with hysteresis

4 Experimental results

The proposed circuits were designed and fabricated using a 0.35-μm CMOS process. A photograph of the designed die is presented in Fig. 10. It has an active area of 705 μm×617 μm. For the experiment, a 3-V source with a 15-kΩ series resistance was used to emulate the TEG device (Fig. 1). The main parameters were V_{OC}=2.96 V, I_{SC}=176 μA, P_{max}=146 μW, V_{MPP}=1.48 V, and R_{Load}=15 kΩ. The selected capacitances were C_{TEG}=10 nF and C_{STO}=47 μF, respectively.

Fig. 11 shows the start-up operation of the circuit. At first, the capacitor C_{TEG} was charged because PMOS SW1 was open. When V_{TEG} reached the

threshold voltage of the PMOS switch, C_{STO} was charged through the switch. The charging rate of C_{STO} was much lower than that of C_{TEG}, because of its higher capacitance. When V_{STO} increased sufficiently for the pulse generator of the MPPT controller to operate, the signal MC was generated, and the band-band control for the MPPT process started. The measured start-up time was 750 ms.
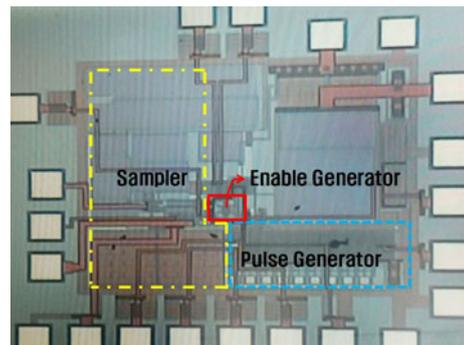

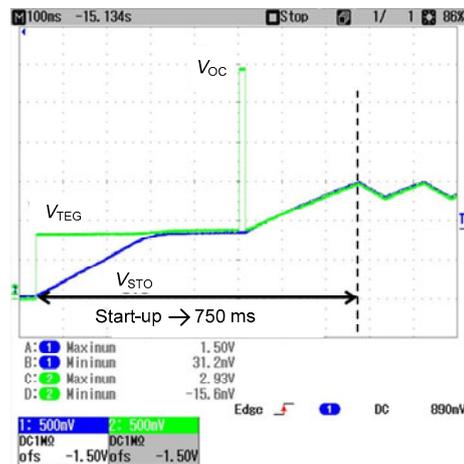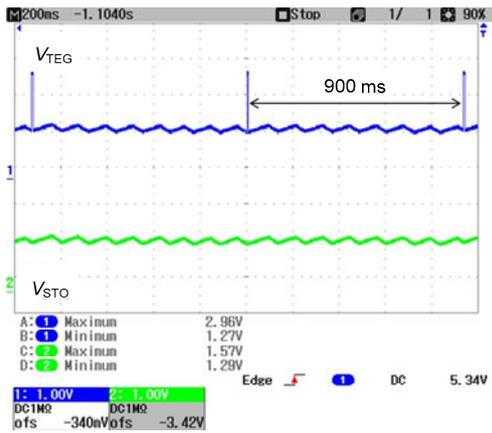**Fig. 10 Photograph of the fabricated die**

Fig. 11 Measured waveforms of V_{TEG} and V_{STO} during the start-up operation

Fig. 12 shows the measured steady-state waveforms of V_{TEG}, V_{STO}, and V_{Load} when the load resistance was 6.2 kΩ. The TEG output voltage reached V_{OC} (=2.96 V) periodically for MPPT control while MC=1. Except for this time period, V_{TEG} (and thus V_{STO}) was maintained around V_{MPP} (1.48 V). V_{TEG} was regulated in 1.36–1.55 V; its average value was hence 1.46 V, a value that very closely approximated V_{MPP}. Also, V_{Load} followed V_{STO} during the discharge phases. The active time, which is the duration of the discharge
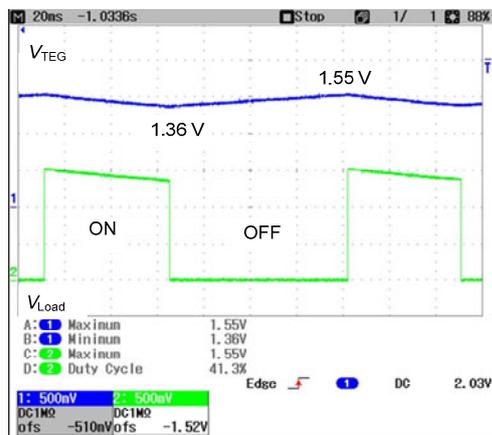
phase, was 50 ms. The active time depends on the size of C_{STO}. As mentioned above, the selected capacitance was 47 µF considering the time limitation for simulation and measurement. If a larger C_{STO} was used, the active time could be increased. Consider the sensor node presented by Kim et al. (2015) which operated from 1.2 V and consumed 36 µW during the active period (700 ms: relatively long compared with the others in Table 1). To satisfy these conditions (36 µW@1.2 V→R_{Load}=40 kΩ) with our circuit using the TEG model (V_T=3 V and R_T=15 kΩ), the required C_{STO} should satisfy

$$
\begin{aligned}
C_{STO} &= \frac{\Delta T \cdot L_{Load}}{\Delta V_{STO}} \\
&= \frac{700\ \text{ms} \,(1.45\ \text{V}\,/\,40\,\text{k}\Omega)}{1.55\ \text{V} - 1.36\ \text{V}} = 133.6\ \text{µF},
\end{aligned}
\tag{3}
$$

where ΔV_{STO} can be checked in Fig. 12.

Fig. 13 shows the measured waveforms of V_{STO} and V_{Load} for different load resistances. The duty cycle (the fraction of the time that power is being delivered to the load) was 3.6% for a 510-Ω load resistor, increasing to 90% when the load resistance increased to 13 kΩ. As the load resistance increased, the power consumed by the load resistor decreased. Thus, the discharging speed decreased and the duty cycle increased.
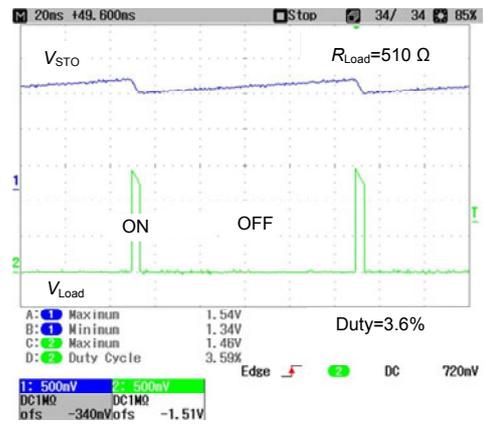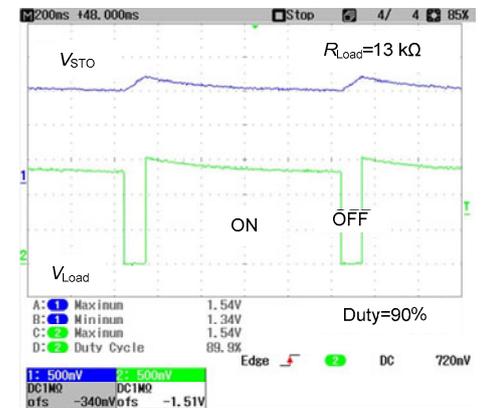

Fig. 12 Measured waveforms of V_{TEG}, V_{STO}, and V_{Load} at steady state: (a) V_{TEG} and V_{STO}; (b) V_{TEG} and V_{Load}

Fig. 13 Measured waveforms of V_{STO} and V_{Load} for different load resistances: (a) 510 Ω; (b) 13 kΩ

Fig. 14 shows the MPPT performance for a varying V_{OC}. V_T (and thus V_{OC}) was changed from 3 V to 5 V and then 3 V to 2 V. The average value of V_{TEG} was 2.47 V for V_T=5 V, and 1.01 V for V_T=2 V. Thus, the designed circuit can track the MPP voltage even in the presence of V_T variations. The transition time for the circuit to settle to new MPP voltages was 350 ms in both cases.
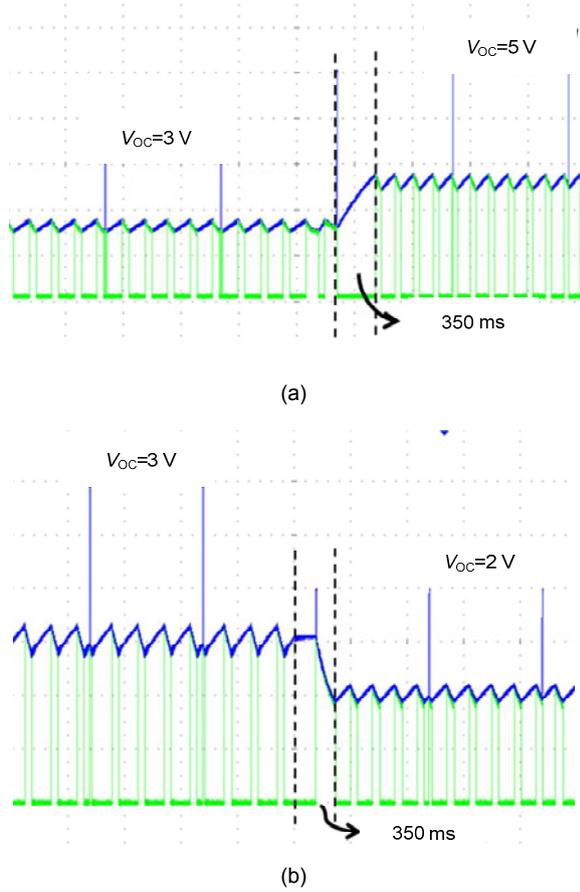
(a)

(b)

Fig. 14 Measured waveforms of the MPPT process with variations in the open-circuit voltage: (a) V_T changes from 3 V to 5 V; (b) V_T changes from 3 V to 2 V

Fig. 15 shows the measured power efficiencies of the designed circuit for different load resistances. The power efficiency is expressed as

$$\frac{P_{Load}}{P_{TEG}} = \frac{\frac{1}{T}\int_0^T [V_{Load}^2(t) / R_{Load}]dt}{\frac{1}{T}\int_0^T [V_{TEG}(t) \cdot I_{TEG}(t)]dt}. \qquad (4)$$

The measured peak power efficiency was 95.5%. The efficiencies were greater than 87% for 500 $\Omega \leq$ $R_{Load} \leq 15$ kΩ. For $R_{Load} > 15$ kΩ, the operation duty cycle became 100%. Therefore, the circuit operated in continuous mode and deviated from MPP, resulting in an efficiency reduction. The MPPT accuracy of the designed circuit is plotted in Fig. 16. P_{max} is the maximum available power of the TEG, as given by Eq. (2). The tracking accuracy was greater than 99%

for the above-mentioned R_{Load} range, demonstrating the good performance of the proposed MPPT scheme. Table 3 shows a comparison of the performance of the presented circuit with state-of-the-art thermal energy harvesting circuits.
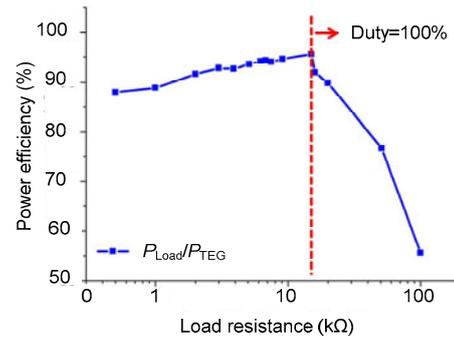

Fig. 15 Power efficiency of the designed circuit versus load resistance
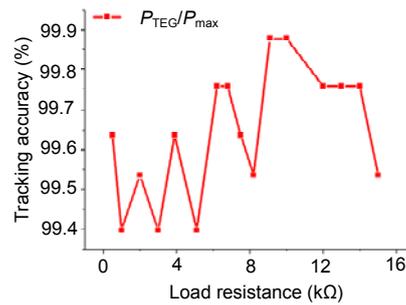

Fig. 16 MPP tracking accuracy of the designed circuit

As mentioned in Section 2, the TEG model (V_T=3 V and R_T=15 kΩ) used for the experiment was equivalent to 17 commercial Thermo Life TEGs wired in parallel, and thus is not suitable for miniature-sized sensor nodes. In this study, however, we aimed to present a simple implementation technique for a thermal energy harvesting circuit targeted for TEG devices with high output voltage. We have verified experimentally that the designed circuit works properly with a TEG model (V_T=3 V and R_T=100 kΩ) corresponding to three commercial TEGs wired in parallel. The proposed circuit can work with a single miniature-sized TEG if the power consumption of the designed circuit is optimized using ultralow-power circuits and techniques, and advanced processes rather than a 0.35 μm process.

Table 3 Performance comparison with state-of-the-art thermal energy harvesting circuits

Research	Process	TEG	V_{in} (V)	Required external voltage (V)	Start-up mechanism	Number of inductors
Lhermet et al. (2008)	0.35 μm CMOS	1 V/ 60 K R_T=90 Ω	1	1.75–4.3[*]	BC with CP	1
Doms et al. (2009)	0.35 μm HV-CMOS	100 μW R_T=100 kΩ	0.6	2	External voltage	0
Doms et al. (2009)	0.13 μm CMOS	None	0.02–0.25[*]	1[*]	External voltage	1
Ramadass and Chandrakasan (2011)	0.35 μm CMOS	25 mV/K R_T=5 Ω	0.035	1.8[*]	BC with mechanical switch	3
Chen et al. (2011b)	65 nm CMOS	None	0.08	1.3	BC with V^{th}-tuned OSC	1
Im et al. (2012)	0.13 μm CMOS	R_T=5 Ω	0.04–0.3[*]	2[*]	Using a transformer	2
Kim and Kim (2013)	0.35 μm BCDMOS	25 mV/K R_T=8 Ω	0.07–0.6[*]	3–5.8	External voltage	1
Weng et al. (2013)	65 nm CMOS	R_T=6.2 Ω	0.05–0.2[*]	1.2[*]	LC-OSC & voltage multiplier	3
Our work	0.35 μm CMOS	R_T=15 kΩ	0.04–0.3[*]	1–2.5	–	0

Research	DC-DC conversion	MPPT	MPPT scheme	Peak efficiency (end-to-end)	Active area (mm^2)
Lhermet et al. (2008)	BC with inductor	No	–	50% (just BC)	3.12
Doms et al. (2009)	CP	Yes	Hill-climbing	70% (just BC)	3.06
Doms et al. (2009)	BC with inductor	No	–	52%	0.12
Ramadass and Chandrakasan (2011)	BC with inductor	Yes[**]	Fixed frequency	58%	1.6
Chen et al. (2011b)	BC with inductor	No	–	60% (just BC)	0.25
Im et al. (2012)	BC with inductor	Yes	FOC	61%	0.09
Kim and Kim (2013)	BC with inductor	Yes	FOC	72.20% (just BC)	1.9
Weng et al. (2013)	BC with inductor	Yes[**]	Fixed frequency	73%	0.98 (w/pads)
Our work	–	Yes	FOC	97.50%	0.43

BC: boost converter; CP: charge pump; OSC: oscillator. [*] V_{oc} (in V); [**] not tracking

5 Conclusions

In this paper we present a simple thermal energy harvesting circuit designed for TEG devices with high output voltage. The circuit operates in active/asleep mode and includes a simple MPPT controller using a FOC technique. The proposed circuit was fabricated using a standard 0.35 μm CMOS process. The results show that the designed circuit can track the MPP voltage even with variations of the V_{OC}. The measured peak power efficiency was 97.5% and MPPT accuracy was greater than 99%. The proposed circuit does not require any external voltages, start-up circuitry, or even DC-DC boosters, which makes it well suited for self-powered miniature-sized sensor node applications.

References

Arsalan M, Ouda MH, Marnat L, et al., 2013. A 5.2GHz, 0.5mW RF powered wireless sensor with dual on-chip antennas for implantable intraocular pressure monitoring. IEEE MTT-S Int Microwave Symp, p.1-4. https://doi.org/10.1109/MWSYM.2013.6697639

Belleville M, Fanet H, Fiorini P, et al., 2010. Energy autonomous sensor systems: towards a ubiquitous sensor technology. *Microelectron J*, 41(11):740-745. https://doi.org/10.1016/j.mejo.2010.01.009

Carlson EJ, Strunz K, Otis BP, 2010. 20 mV input boost converter with efficient digital control for thermoelectric energy harvesting. *IEEE J Sol-State Circ*, 45(4):741-750. https://doi.org/10.1109/JSSC.2010.2042251

Chen PH, Ishida K, Ikeuchi K, et al., 2011a. A 95 mV-startup step-up converter with V^{th}-tuned oscillator by fixed-charge programming and capacitor pass-on scheme. IEEE Int Solid-State Circuits Conf, p.216-217. https://doi.org/10.1109/ISSCC.2011.5746290

Chen PH, Ishida K, Zhang X, et al., 2011b. A 80 mV input, fast startup dual-mode boost converter with charge-pumped pulse generator for energy harvesting. IEEE Asian Solid-State Circuits Conf, p.33-36. https://doi.org/10.1109/ASSCC.2011.6123562

Cheng MH, Wu ZW, 2005. Low-power low-voltage reference using peaking current mirror circuit. *Electron Lett*, 41(10):572-573. https://doi.org/10.1049/el:20050316

Colomer-Farrarons J, Miribel-Catala P, Saiz-Vela A, et al., 2008. Power-conditioning circuitry for a self-powered system based on micro PZT generators in a 0.13 μm low-voltage low-power technology. *IEEE Trans Ind Electron*, 55(9):3249-3257. https://doi.org/10.1109/TIE.2008.927973

Doms I, Merken P, Hoof CV, et al., 2009. Capacitive power management circuit for micropower thermoelectric generators with a 1.4 μA controller. *IEEE J Sol-State Circ*, 44(10):2824-2833. https://doi.org/10.1109/JSSC.2009.2027546

Im JP, Wang SW, Lee KH, et al., 2012. A 40 mV transformer-reuse self-startup boost converter with MPPT control for thermoelectric energy harvesting. *IEEE J Sol-State Circ*, 47(12):3055-3067. https://doi.org/10.1109/JSSC.2012.2225734

Jang JH, Berdy DF, Lee JJ, et al., 2013. A wireless condition monitoring system powered by a sub-100 μW vibration energy harvester. *IEEE Trans Circ Syst*, 60(4):1082-1093. https://doi.org/10.1109/TCSI.2012.2215395

Kausar ASMZ, Reza AW, Saleh MU, et al., 2014. Energizing wireless sensor networks by energy harvesting systems: scopes, challenges and approaches. *Renew Sustain Energy Rev*, 38:973-989. https://doi.org/10.1016/j.rser.2014.07.035

Kim HS, Kim GH, Lee YM, et al., 2015. A 10.6 mm³ fully-integrated, wireless sensor node with 8GHz UWB transmitter. Symp on VLSI Circuits, p.202-203. https://doi.org/10.1109/VLSIC.2015.7231258

Kim J, Kim C, 2013. A DC-DC boost converter with variation tolerant MPPT technique and efficient ZCS circuit for thermoelectric energy harvesting applications. *IEEE Trans Power Electron*, 28(8):3827-3833. https://doi.org/10.1109/TPEL.2012.2231098

Kim RY, Lai JS, 2008. A seamless mode transfer maximum power point tracking controller for thermoelectric generator applications. *IEEE Trans Power Electron*, 23(5):2310-2318. https://doi.org/10.1109/TPEL.2008.2001904

Lee YM, Bang SY, Lee IH, et al., 2013. A modular 1 mm³ die-stacked sensing platform with low power I²C inter-die communication and multi-modal energy harvesting. *IEEE J Sol-State Circ*, 48(1):229-243. https://doi.org/10.1109/JSSC.2012.2221233

Leonov V, Fiorini P, Sedky S, et al., 2005. Thermoelectric MEMS generators as a power supply for a body area network. 13th Int Conf on Solid-State Sensors, Actuators and Microsystems, p.291-294. https://doi.org/10.1109/SENSOR.2005.1496414

Lhermet H, Condemine C, Plissonnier M, et al., 2008. Efficient power management circuit: from thermal energy harvesting to above-IC microbattery energy storage. *IEEE J Sol-State Circ*, 43(1):246-255. https://doi.org/10.1109/JSSC.2007.914725

Li W, Yao R, Guo L, 2009. A low power CMOS bandgap voltage reference with enhanced power supply rejection. 8th Int Conf on ASIC, p.300-304. https://doi.org/10.1109/ASICON.2009.5351450

Lu C, Tsui CY, Ki WH, 2011. Vibration energy scavenging system with maximum power tracking for micropower applications. *IEEE Trans VLSI Syst*, 19(11):2109-2119. https://doi.org/10.1109/TVLSI.2010.2069574

Mansano AL, Li YJ, Bagga S, et al., 2016. An autonomous wireless sensor node with asynchronous ECG monitoring in 0.18 μm CMOS. *IEEE Trans Biomed Circ Syst*, 10(3):602-611. https://doi.org/10.1109/TBCAS.2015.2495272

Micropelt, 2018. Thin film Thermogenerator, MPG-D655. http://www.micropelt.com

Morimura H, Oshima S, Matsunaga K, et al., 2014. Ultra-low-power circuit techniques for mm-size wireless sensor nodes with energy harvesting. *IEICE Electron Exp*, 11(20):1-12.
https://doi.org/10.1587/elex.11.20142009

Ramadass YK, Chandrakasan AP, 2011. A battery-less thermoelectric energy harvesting interface circuit with 35 mV startup voltage. *IEEE J Sol-State Circ*, 46(1):333-341.
https://doi.org/10.1109/JSSC.2010.2074090

Seeman MD, Sanders SR, Rabaey JM, 2008. An ultra-low-power power management IC for energy-scavenged wireless sensor nodes. IEEE Power Electronics Specialists Conf, p.925-931.
https://doi.org/10.1109/PESC.2008.4592048

Strasser M, Aigner R, Lauterbach C, et al., 2003. Micro-machined CMOS thermoelectric generators as on-chip power supply. 12th Int Conf on Solid-State Sensors, Actuators and Microsystems, p.45-48.
https://doi.org/10.1109/SENSOR.2003.1215249

Weng PS, Tang HY, Ku PC, et al., 2013. 50 mV-input batteryless boost converter for thermal energy harvesting. *IEEE J Sol-State Circ*, 48(4):1031-1041.
https://doi.org/10.1109/JSSC.2013.2237998

Yoon EJ, Yu CG, 2016. Power management circuits for self-powered systems based on micro-scale solar energy harvesting. *Int J Electron*, 103(3):516-529.
https://doi.org/10.1080/00207217.2015.1036802

Zhang Y, Zhang F, Shakhsheer Y, et al., 2013. A batteryless 19 μW MICS/ISM-band energy harvesting body sensor node SoC for ExG applications. *IEEE J Sol-State Circ*, 48(1):199-213.
https://doi.org/10.1109/JSSC.2012.2221217